What drives the velocity dispersion of ionized gas in star-forming galaxies?

Xiaoling Yu [1,2] Yong Shi [1,2]★ Yanmei Chen,[1,2] David R. Law,[3] Dmitry Bizyaev,[4,5] Longji Bing [1,2] Songlin Li [1,2] Luwenjia Zhou,[1,2] Jianhang Chen,[1,2] Rogemar A. Riffel [6,7] Rogério Riffel [7,8] Kai Zhang,[9] Yongyun Chen[1,2] and Kaike Pan[4]

[1]*School of Astronomy and Space Science, Nanjing University, Nanjing 210093, China*
[2]*Key Laboratory of Modern Astronomy and Astrophysics (Nanjing University), Ministry of Education, Nanjing 210093, China*
[3]*Space Telescope Science Institute, 3700 San Martin Drive, Baltimore, MD 21218, USA*
[4]*Apache Point Observatory and New Mexico State University, PO Box 59, Sunspot, NM 88349-0059, USA*
[5]*Sternberg Astronomical Institute, Moscow State University, Moscow 119234, Russia*
[6]*Departamento de Física, CCNE, Universidade Federal de Santa Maria, 97105-900 Santa Maria, RS, Brazil*
[7]*Laboratório Interinstitucional de e-Astronomia, Rua General José Cristino, 77 Vasco da Gama, Rio de Janeiro 20921-400, Brazil*
[8]*Departamento de Astronomia, Universidade Federal do Rio Grandedo Sul - Av. Bento Gonçalves 9500, Porto Alegre, RS, Brazil*
[9]*Department of Physics and Astronomy, University of Kentucky, 505 Rose Street, Lexington, KY 40506, USA*

ABSTRACT

We analyse the intrinsic velocity dispersion properties of 648 star-forming galaxies observed by the Mapping Nearby Galaxies at Apache Point Observatory (MaNGA) survey, to explore the relation of intrinsic gas velocity dispersions with star formation rates (SFRs), SFR surface densities (Σ_{SFR}), stellar masses, and stellar mass surface densities (Σ_*). By combining with high z galaxies, we found that there is a good correlation between the velocity dispersion and the SFR as well as Σ_{SFR}. But the correlation between the velocity dispersion and the stellar mass as well as Σ_* is moderate. By comparing our results with predictions of theoretical models, we found that the energy feedback from star formation processes alone and the gravitational instability alone cannot fully explain simultaneously the observed velocity–dispersion/SFR and velocity–dispersion/Σ_{SFR} relationships.

Key words: galaxies: evolution – galaxies: ISM – galaxies: kinematics and dynamics – galaxies: star formation.

1 INTRODUCTION

It is well known that the cosmic star formation rate (SFR) peaks around the redshift of ∼1–3 (Lilly et al. 1996; Madau et al. 1996; Hopkins & Beacom 2006; Karim et al. 2011; Burgarella et al. 2013; Sobral et al. 2013; Madau & Dickinson 2014). A key question is to understand what drives this evolution. Studies of spatially resolved ionized-gas kinematics are powerful tools to characterize the galactic dynamics and their roles in driving the evolution of cosmic star formation.

High gas velocity dispersion seems to be a common feature of galaxies at high redshift. The supersonic velocity dispersion implies a highly turbulent interstellar medium (ISM) of distant galaxies (Law et al. 2007; Förster Schreiber et al. 2009; Elmegreen & Burkert 2010; Green et al. 2014; Simons et al. 2017; Johnson et al. 2018). Theoretical and observational studies also suggest that gas of distant galaxies has larger random motions compared to that in low-

redshift galaxies (Nesvadba et al. 2006; Lehnert et al. 2009, 2013; Green et al. 2010, 2014; Wisnioski et al. 2015; Zhou et al. 2017; Johnson et al. 2018). These highly turbulent motions may play a crucial role in star formation (Green et al. 2010, 2014; Federrath & Klessen 2012; Zhou et al. 2017). Since the turbulence in the ISM decays quickly, some source of energy is required to maintain it (Mac Low et al. 1998; Stone, Ostriker & Gammie 1998; Mac Low 1999; Green et al. 2014; Johnson et al. 2018). Both external and internal mechanisms have been suggested. The former includes gas accretion from the intergalactic medium and minor mergers (Glazebrook 2013), while the latter invokes star formation feedback (Lehnert et al. 2009, 2013; Green et al. 2010, 2014; Le Tiran et al. 2011), initial gravitational collapse (Elmegreen & Burkert 2010), gravitational disc instabilities (Bournaud et al. 2010, 2014; Goldbaum, Krumholz & Forbes 2015), cloud–cloud collisions in the disk (Tasker & Tan 2009), galactic shear from differential rotation in disk galaxies (Krumholz & Burkhart 2016), and some combinations of the above effects.

Green et al. (2010, 2014) found that there is a correlation between the star formation rate (SFR) and gas velocity dispersion

★ E-mail: yong@nju.edu.cn

in both local and high-redshift star-forming galaxies. Lehnert et al. (2009, 2013) further showed that the SFR surface density (Σ_{SFR}) is also related with the gas velocity dispersion in active star-forming galaxies at $z \sim 1$–3, consistent with that star formation feedback supports the high gas velocity dispersions and balances the gravitational force. On the other hand, Johnson et al. (2018) found there is a weak trend between the SFR and gas velocity dispersion for both local and high-redshift galaxies. For individual star-forming clumps at $z \sim 2$, Genzel et al. (2011) did not found a strong trend between Σ_{SFR} and gas velocity dispersion either, and suggested that a large-scale release of gravitational energy could induce the global large random motions in high-z galaxies.

In this paper, we took advantage of a large sample of local star-forming galaxies with 2-D spectroscopic data available in Mapping Nearby Galaxies at Apache Point Observatory (MaNGA, Bundy et al. 2015), to investigate the relationship between gas velocity dispersions and SFRs as well as stellar masses. Compared to other Integral Field Spectroscopy (IFS) surveys, such as Calar Alto Legacy Integral Field Area (CALIFA) survey (Sánchez et al. 2012), Sydney-AAO Multi-object Integral field spectrograph (SAMI) Galaxy Survey (Croom et al. 2012; Bryant et al. 2014), MaNGA covers a wide wavelength range from 3600 Å to 10 300 Å for a sample of eventually 10 000 nearby galaxies. In this paper, we used 2700 galaxies already released by MaNGA Product Launch-5 (MPL-5). We further collected the SFR, Σ_{SFR}, and gas velocity dispersion data of high-z galaxies from the literatures.

In Section 2, we describe the MaNGA survey, the sample selection criteria, and data reduction strategy. Section 3 presents our MaNGA sample results and compares with high-redshift samples. We discuss which physical processes may drive turbulence in the ISM, and compare with theoretical models in Section 4. In Section 5, we summarize our main conclusions. We use the cosmological parameters $H_0 = 70$ km s^{-1} Mpc^{-1}, $\Omega_m = 0.3$, $\Omega_\Lambda = 0.7$ throughout this paper.

2 DATA

2.1 The MaNGA data

The MaNGA survey is one of three core programmes in the fourth generation of the Sloan Digital Sky Survey (SDSS-IV) that began on July 1, 2014 and aims to obtain spatially resolved information of nearly 10 000 galaxies by 2020 (Bundy et al. 2015; Drory et al. 2015; Law et al. 2015; Yan et al. 2016a; Blanton et al. 2017), which is observed by the 2.5 m Sloan Telescope (Gunn et al. 2006). MaNGA is designed to investigate the internal kinematic structure and composition of gas and stars for a large sample of nearby galaxies at a spatial resolution of 2.5 arcsec ($\sim$1 kpc). MaNGA employs dithered observations that contain 17 hexagonal bundles of 2$''$ fibres with five sizes: $2 \times N_{19}$ (12 arcsec in diameter), $4 \times N_{37}$, $4 \times N_{61}$, $2 \times N_{91}$, $5 \times N_{127}$ (32 arcsec in diameter). It provides resolved spectroscopy over a wide wavelength range from 3600 Å to 10300 Å at R $\sim$ 2,000 (Smee et al. 2013; Jin et al. 2016; Yan et al. 2016a).

The MaNGA sample is volume limited within a redshift range of 0.01 $\sim$ 0.15 (Wake et al. 2017), and it is composed of 'Primary' and 'Secondary' samples based on the spatial extent of the observational coverage. The 'Primary' sample contains two-thirds of the targets with the observations extended to 1.5 R_e and the 'Secondary' sample contains the remaining one-third with the observations out to 2.5 R_e. The observations were designed to provide signal-to-noise ratio of 5 or better in the stellar spectrum
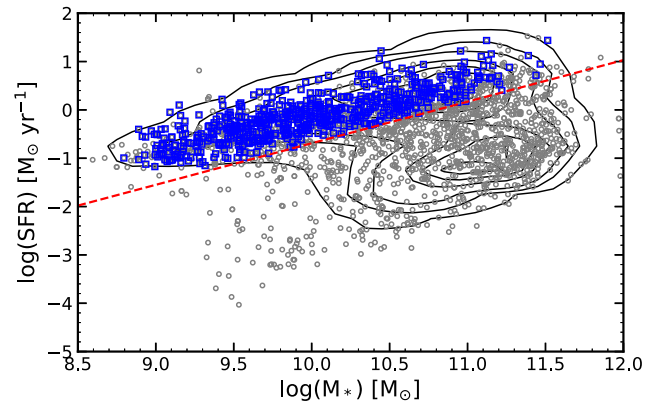

Figure 1. The star formation rate versus stellar mass diagram of 2360 MaNGA galaxies. Contours show the GSWLC sample. The grey open circles represent 2360 MaNGA galaxies. The red dashed line is adopted as an approximation of the boundary of the star-forming main sequence. The blue open squares represent 648 star-forming galaxies, which the stack spectrums of Hα emission lines are fitting well.

within the limits given above (Yan et al. 2016b). The raw data reduction is described in Law et al. (2016). The current study includes 2716 galaxies that have been observed by MaNGA till the summer of 2016, which were from MPL-5.

2.2 Sample selection and spectral fitting

We first cross-matched our MaNGA galaxies with GALEX-SDSS-WISE Legacy Catalogue (GSWLC) (Salim et al. 2016) to obtain the global stellar mass and SFR for 2360 galaxies as shown in Fig. 1. The red dashed line is adopted from fig. 11 of Chang et al. (2015) as an approximation of the boundary (at the 1σ level in scatter) of the star-forming main sequence (Chen et al. 2016). Jin et al. (2016) gives the approximate slope and intercept (log SFR > $0.86 \times \log M_* - 9.29$). Totally with 1221 star-forming galaxies. We classified these galaxies into pure star-formation galaxies, AGN and LINERs according to the BPT diagrams with some examples shown in fig. 2 (Baldwin, Phillips & Terlevich 1981; Kauffmann et al. 2003; Kewley et al. 2006). The fractions of AGN and LINER nature are about 4.42 per cent (52 of 1221). These sources may be influenced by shocks (Kewley et al. 2013; Harrison et al. 2016; Johnson et al. 2018), and their SFRs cannot be estimated accurately. We thus removed them from the further study. Merging galaxies as identified in the SDSS image were excluded further (e.g. the third row in Fig. 2). We further selected the relatively face on galaxies, which the axial ratio more than 0.5 ($b/a > 0.5$). The axis ratios and effective radius are from the data release by MaNGA[1] (Westfall et al. 2019).

For each galaxy in our final selected sample, we stacked the spectrum of all spaxels that are not flagged by MaNGA Data Analysis Pipeline (DAP, Westfall et al., in preparation) Pixel Mask to obtain the total flux of each galaxy. During stacking, we didn't shift the emission in the spaxels according to the spatially resolved velocity information. We then fitted it to derive the underlying stellar component with the code of Penalized Pixel-Fitting (pPXF) using MILES templates (Cappellari 2017; Cappellari & Emsellem 2004), as shown in Fig. 3. We then used the IDL code of MPFITEXPR to fit the remaining nebular spectra with single Gaussian profiles as

---

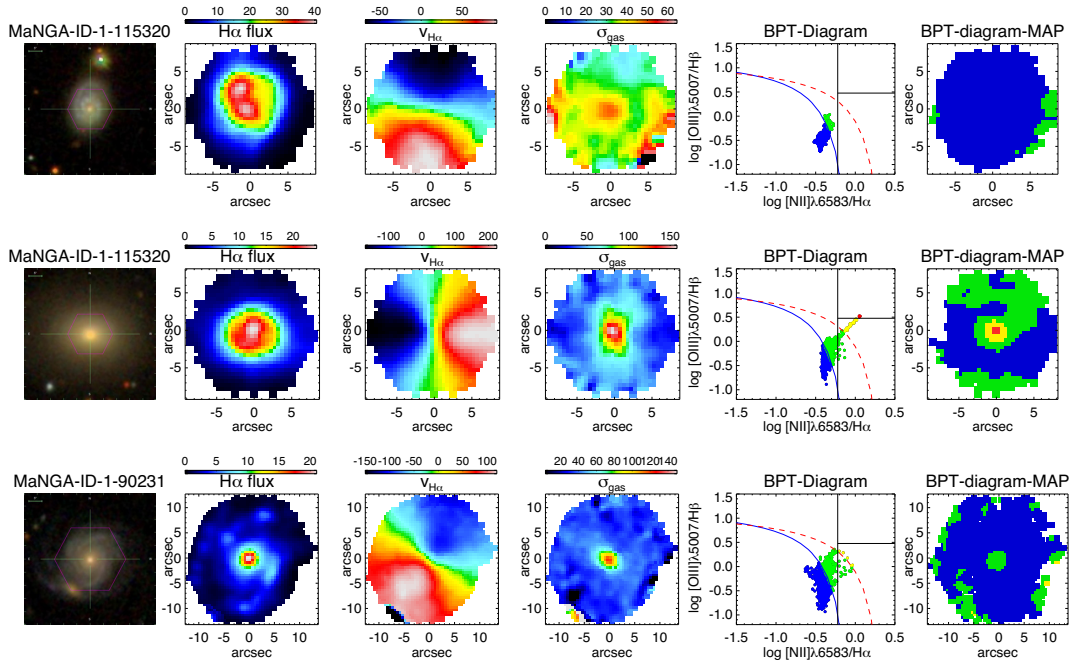[1] https://dr15.sdss.org/sas/dr15/manga/spectro/analysis/v2_4_3/2.2.1/

Figure 2. Three examples of MaNGA galaxies, which are representative of three types of strong Hα emission lines. The first column shows the SDSS g, r, i−band image, the Hα flux maps are shown in the second column, while the Hα flux is in unit of 10^{-17} erg s^{-1} cm^{-2}. The third and fourth columns show the gas velocity and gas velocity dispersion fields, respectively. In the third column, the red side is moving away from us and the blue side is approaching.The last tow columns show the BPT diagrams and the maps of BPT diagram, while the blue solid curve and the red dashed curve are the boundary of star formation, composite and AGN regions. The blue region is representative of the star formation region, the green region representative of the composite region. The remaining region is contributed by AGN, while the yellow colour and the red colour are representative of the region of low-ionization nuclear emission regions (LINERs) and Seyferts. The spatial resolved informations (all the flux of emission lines, Hα velocity, and Hα velocity dispersions) are obtained by fitting the emission lines with the MaNGA DAP pipeline (Westfall et al. 2019).

shown in Fig. 3. During the fitting, we further excluded 98 galaxies with weak emission lines and 48 galaxies with poor fitting. From each fitting, we measured the flux and the ionized gas velocity dispersion of the Hα emission lines. At this step, we corrected effect of the beam smearing on the derived velocity dispersion. More details are in Section 2.4.1. The final sample contains 648 star-forming galaxies shown as blue open squares in Fig. 1.

2.3 Star formation rate (SFR)

From the spectral fitting, we also derived the Hα and Hβ flux to estimate the extinction under the case B (Calzetti 2001). The spatial-resolved SFRs are then estimated from the extinction-corrected Hα luminosities (Kennicutt 1998) with a Chabrier IMF (Chabrier 2003):

$$\mathrm{SFR}(\mathrm{M_\odot\ yr^{-1}}) = 0.56 \times 7.9 \times 10^{-42} L_{\mathrm{H\alpha,int}}\ (\mathrm{erg\ s^{-1}}) \qquad (1)$$

2.4 Gas velocity dispersion

Ionized gas velocity dispersion (σ_{gas}) is measured from the Hα line. The gas velocity dispersion needs to remove the instrument resolutions, i.e. $\sigma_{\mathrm{gas}} = (\sigma_{\mathrm{obs}}^2 - \sigma_{\mathrm{instr}}^2)^{1/2}$, where σ_{instr} is the instrumental velocity dispersion and σ_{obs} is the observed velocity dispersion. For the single pixel of each galaxy, MaNGA data analysis pipeline provided the σ_{instr}. We used the mean σ_{instr} value of all spaxels.

2.4.1 The Effect of Beam Smearing

The measured gas velocity dispersion may be overestimated in the presence of a velocity gradient. As Integral Field Unit (IFU)

observations are convolved with the point spread function (PSF), information from each spatial pixel is blended with that of neighbouring regions. This is so called 'beam smearing' (Epinat et al. 2010; Davies et al. 2011; Johnson et al. 2018; Zhou et al. 2017). The effect is to artificially increase the observed velocity dispersion, particularly at the dynamical centre.

To remove the beam smearing, Green et al. (2010) provided an empirical approach based on the observed velocity map. Following their approach, we first constructed a Hα flux map and its velocity map with five times higher spatial resolution using a linear interpolation according to the observed maps. According to the interpolated flux and velocity maps, we constructed an artificial spectrum with a single Gaussian profile at each location. The instrumental resolution is adopted as the velocity dispersion of the model spectrum. Then we convolved this artificial IFU data with a 2D Gaussian kernel with the FWHM equal to the seeing for each observation, and binned this high resolution data cube back to the original observational resolution, and measured their velocity dispersion (σ_{smear}). The final derived dispersion is $\sigma_{\mathrm{gas,correct}} = (\sigma_{\mathrm{gas}}^2 - \sigma_{\mathrm{smear}}^2)^{1/2}$. Fig. 4 shows the effect of beam smearing on σ_{gas}.

2.4.2 The effect of instrumental Line Spread Function (LSF)

The spectral resolution of MaNGA is $50 \sim 80$ km s^{-1} (Bundy et al. 2015). Because of the Instrumental LSF, the σ_{gas} may have large uncertainties or even systematic offsets given inaccurate estimate of the instrumental LSF. The Sydney-AAO Multi-object Integral field spectrograph (SAMI) Galaxy Survey have released the first version data (Green et al. 2018), with a higher spectral resolution of 29
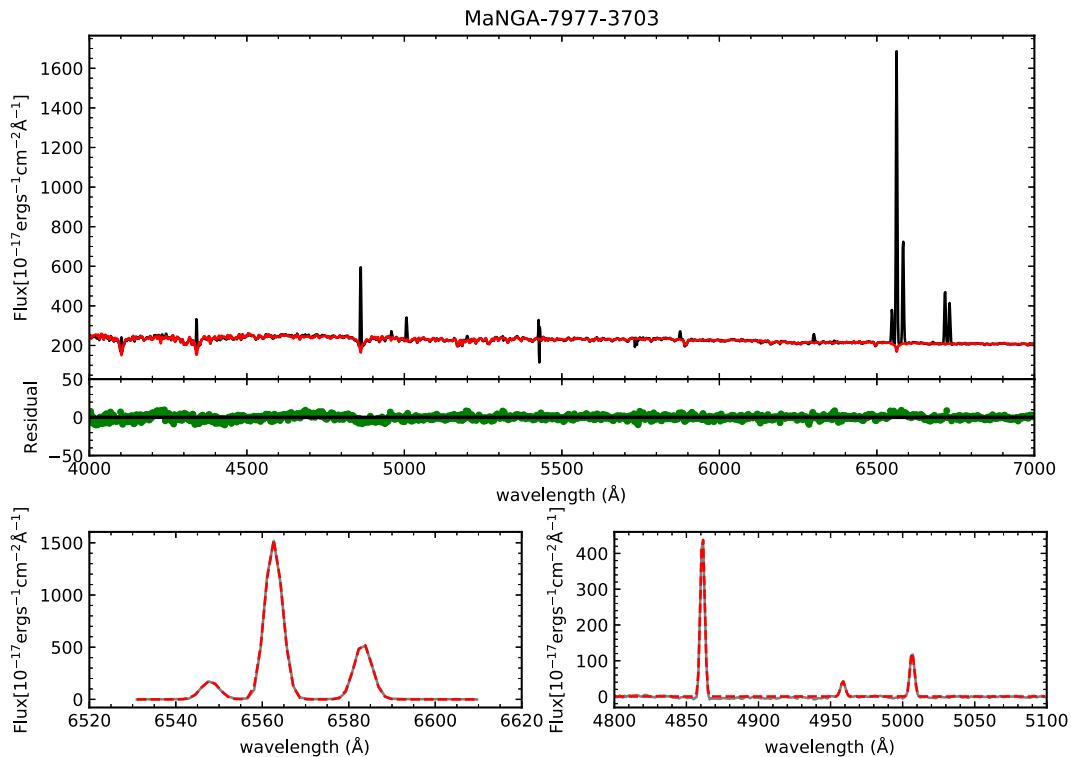
Figure 3. Top: An example galaxy of stellar and gas kinematics fit with pPXF. The black line is the relative flux of the observed spectrum. The red line is the pPXF fit for the stellar component. Residuals are presented in the middle plane (green symbols). Bottom: An example galaxy of spectral fitting. The grey line is the stack flux of the observed spectrum. The red dashed line is the best-fitting spectrum of Gaussian using IDL code of MPFITEXPR. The left panel shows the Hα region fitting and the right panel shows the Hβ region fitting.
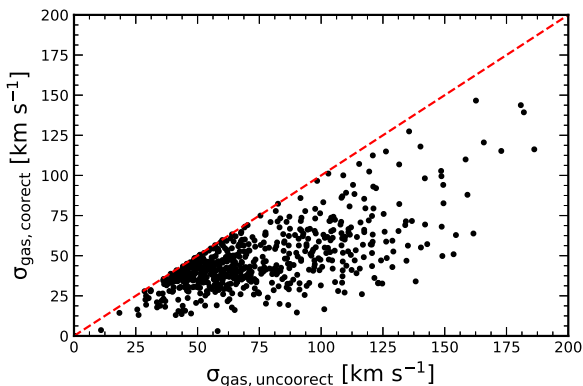

Figure 4. Effect of beam smearing on σ_{gas}. We plot the results of modelling the effect of beam-smearing on our measure of velocity dispersion and removing it. The *x*-axis shows the σ_{gas}, which is the uncorrected effect of beam smearing. The *y*-axis shows the σ_{gas} corrected for beam smearing. The dashed red line shows the one-to-one relation.
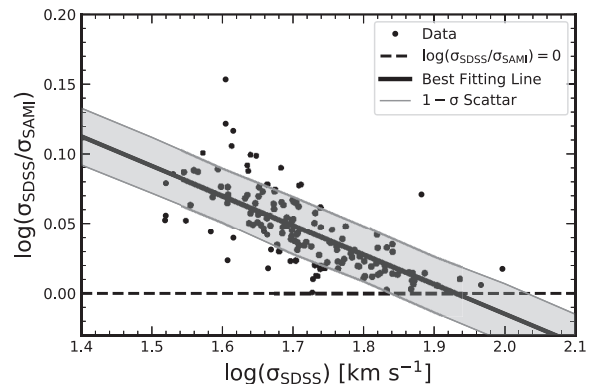

Figure 5. The ratio of velocity dispersions measured for SAMI galaxies degraded to the MaNGA resolutions to that at the SAMI resolution. The black solid line refers to the best fitting line of $\log(\sigma_{SDSS}/\sigma_{SAMI})$ as a function of $\log(\sigma_{SDSS})$. The grey shade region refer to the $1-\sigma$ scatter of the best fit line. The black dashed line refers to $\sigma_{SDSS}/\sigma_{SAMI}$ equal 1.

km s^{-1} at 6250–7350 Å (Green et al. 2018; Sharp et al. 2015; Zhou et al. 2017).

For about 150 published SAMI galaxies, we performed the same measurement as MaNGA galaxies, which is to stack the spectrum of all good spaxels, fit the spectrum with pPXF to get the pure Hα emission line, and fit the profile by a Gaussian curve to derive the velocity dispersion (σ_{SAMI}). We then degraded the stacked spectra of SAMI galaxies to the MaNGA spectral resolution and derived the line width again (σ_{SDSS}). Fig. 5 plots $\sigma_{SDSS}/\sigma_{SAMI}$ versus σ_{SDSS} for the SAMI galaxies. A linear function is fitted to the data with

the best-fitted result as:

$$\log\left(\frac{\sigma_{SDSS}}{\sigma_{SAMI}}\right) = (-0.21 \pm 0.05)\log(\sigma_{SDSS}) + (0.41 \pm 0.09) \quad (2)$$

As shown in the Fig. 5, for σ_{SDSS} larger than 80 km s^{-1}, σ_{SDSS} is equal to σ_{SAMI}. For our MaNGA galaxies with σ_{gas} less than 80 km s^{-1}, we thus used formula (2) to correct the effect of the limited spectral resolution.

Table 1. The results of the linear correlation analysis.

| | $\sigma - \mathrm{SFR}$ | | | $\sigma - \mathrm{M_*}$ | | | $\sigma - \Sigma_{\mathrm{SFR}}$ | | | $\sigma - \Sigma_*$ | | |
	R_S	P	R_B	R_S	P	R_B	R_S	P	R_B	R_S	P	R_B
MaNGA[a]	0.37	<0.001	0.39	0.40	<0.001	0.40	–	–	–	–	–	–
MaNGA[b]	0.39	<0.001	0.38	0.44	<0.001	0.44	0.54	<0.001	0.52	0.63	<0.001	0.60

Notes: [a] Stellar mass and SFR are the total Stellar mass and SFR of galaxies from Salim et al. (2016).
[b] The SFR and Stellar mass within MaNGA FOV. The Σ_{SFR} and Σ_* also just cover the observation region of MaNGA.
R_S: Spearman correlation coefficient.
P: Significance level of the Spearman correlation coefficient.
R_B: Correlation coefficient using the method of Kelly (2007)

Table 2. List the data sources of detail informations for High z and local galaxies.

ref[a]	z	σ[b]	SFR[c]	$M_*^{(d)}$	Σ_{SFR} and $\Sigma_*^{(e)}$	$Beam\,Smearing$[f]
Wisnioski et al. (2011)	$z \sim 1.3$	$H\alpha$	$H\alpha$	SED Fitting	Re	Yes
Swinbank et al. (2012)	$z \sim 0.8–2.2$	$H\alpha$	$H\alpha$	SED Fitting	Re	Yes
Förster Schreiber et al. (2009)	$z \sim 2$	$H\alpha$	$H\alpha$	SED Fitting	Re	Yes
Cresci et al. (2009)	$z \sim 2$	$H\alpha$	$H\alpha$	SED Fitting	R_d	Yes
Lehnert et al. (2013)	$z \sim 1–3$	$H\alpha$	$H\alpha$	–	R_{iso}	Yes
Law et al. (2009)	$z \sim 2–3$	$H\alpha$	$H\alpha$	SED Fitting	R_{ne}	Yes
KMOS-KROSS(Johnson et al. (2018))	$z \sim 1$	$H\alpha$	$H\alpha$	SED Fitting	Re	Yes
DYNAMO((Green et al. 2014))	$z \sim 0.1$	$H\alpha$	$H\alpha$	SED Fitting	Re	Yes

Notes: [a] The references of other high z and local galaxies data sources.
[b] The way of measured gas velocity dispersion. $H\alpha$ means used $H\alpha$ emission lines obtain the σ.
[c] The way of measured SFR. $H\alpha$ means used $H\alpha$ emission lines measured the SFR.
[d] The way of measured Stellar Mass. SED Fitting means used the theory of SED Fitting to measure the Stellar Mass
[e] The way of measured Σ_{SFR} and Σ_*, we used the SFR and stellar mass to divide the area within a defined radius to obtain the Σ_{SFR} and Σ_*. Re means the effective radius. R_d means the radius of the disk scale length. R_{iso} means the radius of isophotal area (the total area of all pixels above the 3σ surface brightness limit of the data). R_{ne} means radius of nebular emission.
[f] Whether or not considering the effect of beam smearing.

2.5 Total stellar mass and surface density of stellar mass

We cross-match GSWLC (Salim et al. 2016) with MaNGA galaxies to obtain the total stellar mass for our sample. The spatially resolved stellar masses are from PIPE3D (Sánchez et al. 2016a,b).

3 RESULTS

3.1 Results for MaNGA Galaxies

As shown in Fig. 6, there is a moderate correlation (Table 1) between the velocity dispersion and the total SFR (top left) and the SFR within MaNGA FOV (top middle), while the relationship with the Σ_{SFR}(top right) is stronger, with a correlation coefficient more than 0.5. There is also a moderate correlation between the velocity dispersion and stellar mass (bottom left and bottom middle), while the relationship with Σ_* is even stronger than that with Σ_{SFR} (see Table 1).

Green et al. (2010) found that the velocity dispersion is correlated with the SFR, but not with the stellar mass or gas fraction. Johnson et al. (2018) analysed about 472 $z \sim 0.9$ star-forming galaxies observed as part of KMOSS Redshift One Spectroscopic Survey (KROSS), and found that the relation between velocity dispersion and SFR was stronger than that between velocity dispersion and stellar mass. For our MaNGA galaxies, we find a good correlation between the velocity dispersion and Σ_{SFR}, and a stronger one with Σ_*.

3.2 Results for MaNGA Galaxies and high-z Galaxies

In this section, we combined our MaNGA galaxies with those at high-redshift. The high-z galaxies are from Wisnioski et al. (2011) ($z \sim 1.3$), Swinbank et al. (2012) ($z \sim 0.8–2.2$), Förster Schreiber et al. (2009) ($z \sim 2$), Cresci et al. (2009) ($z \sim 2$),Lehnert et al. (2013) ($z \sim 1–3$), Law et al. (2009) ($z \sim 2–3$). The KMOS–KROSS sample ($z \sim 1$) is from Johnson et al. (2018). We also included the local DYnamics of Newly-Assembled Massive Objects (DYNAMO) sample ($z \sim 0.1$) (Green et al. 2014) and a sample of nearby dwarf galaxies from Moiseev, Tikhonov & Klypin (2015). Table 2 lists the detailed informations for these studies. From Fig. 7 and Table 3, we found that there is a good correlation between velocity dispersion and SFR as well as Σ_{SFR}. But the correlations with stellar mass and Σ_* are much poorer, in contrast to the case when only considering the MaNGA sample, which is likely caused by the limited dynamic range of MaNGA galaxies only.

4 DISCUSSION

4.1 Which is more fundamental for the relationship with the gas velocity dispersion: SFR or stellar mass?

Many studies in the literature have been done to discuss which one (SFR versus stellar mass) is better related with the gas velocity dispersion. We will go through these works in the following and conclude which one may be more fundamental in driving the gas velocity dispersion.

For the relationship between the velocity dispersion and stellar mass, some studies expected this correlation to exist, because velocity dispersions measure the dynamical support of galaxies, regardless of morphological types (Johnson et al. 2018). Stott et al. (2016) used KROSS sample around redshift of 1.0, and found a weak trend between intrinsic gas velocity dispersion
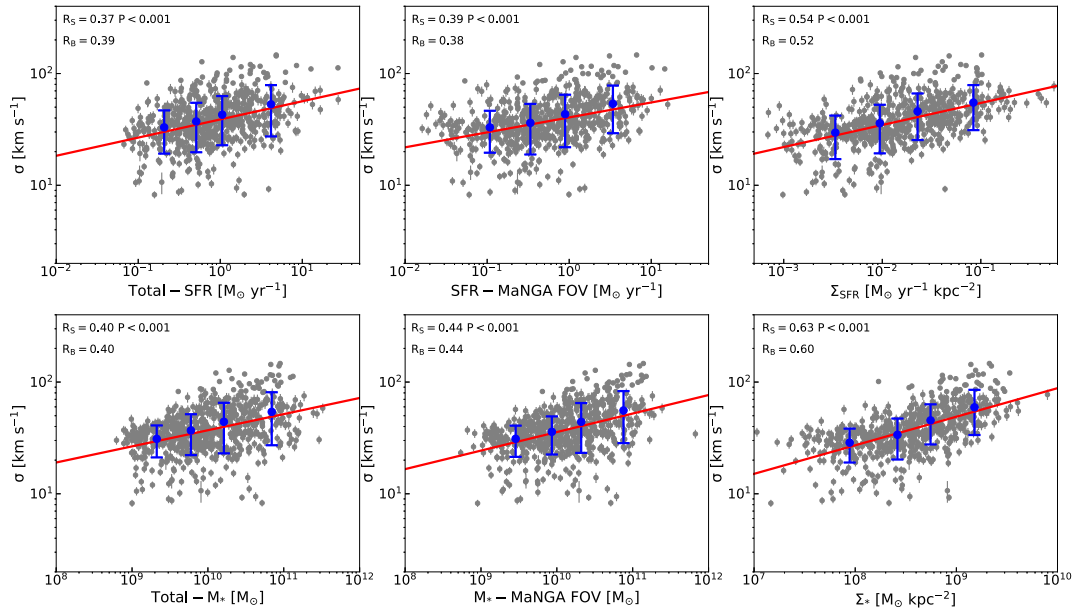
Figure 6. Top: between intrinsic gas velocity dispersion and SFR (top left and top middle) as well as Σ_{SFR}(top right) in Section 3.1. The small grey points show all our selected MaNGA sources. The big blue points and error bars show the value of mean σ and standard deviation in x-axis bins (each containing 25 per cent of our MaNGA sample). The red solid lines show the best Linear Regression fitting of all our selected MaNGA sources using the method of Kelly (2007). In the upper left corner in each panel, R_S represents the Spearman correlation coefficient and R_B represents the corresponding correlation coefficient using the method of Kelly (2007). The Total-SFR from Salim et al. (2016), and the SFR-MaNGA FOV from the emission lines fitting of (Hα region). The Σ_{SFR} are converted from SFR-MaNGA FOV. Bottom: Trends between intrinsic gas velocity dispersion and stellar mass(bottom left and bottom middle) as well as Σ_*(bottom right) in Section 3.1. All symbols and lines are as same as the top panels. The Total $- M_*$ from Salim et al. (2016). The M_*-MaNGA FOV and the Σ_* are converted by PIPE3D (Sánchez et al. 2016a,b).
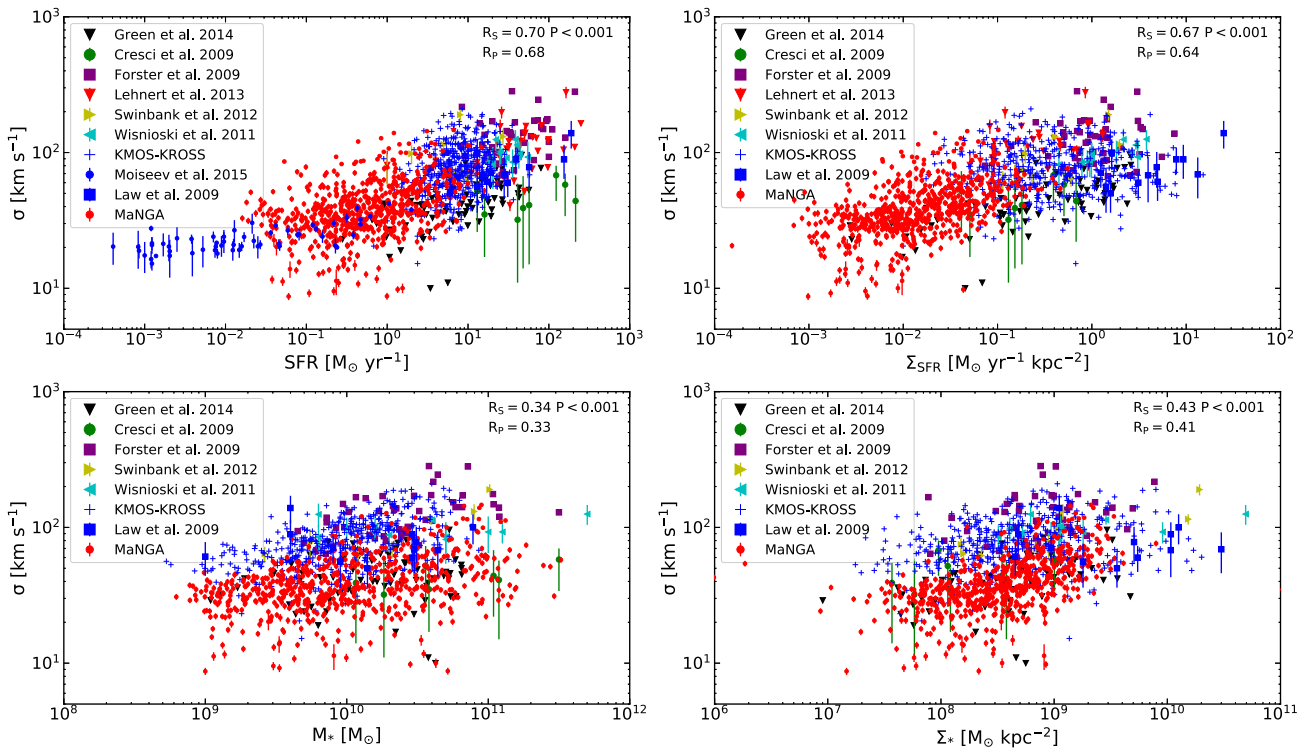

Figure 7. Trends between intrinsic gas velocity dispersion (σ_{gas}) and SFR, Σ_{SFR}, Stellar mass, and Σ_* in Section 3.2. The high-z galaxies are from Wisnioski et al. (2011), Swinbank et al. (2012), Förster Schreiber et al. (2009), Cresci et al. (2009),Lehnert et al. (2013), Gonçalves et al. (2010), and Law et al. (2009). The KMOS–KROSS sample is from Johnson et al. (2018). We also combine the local DYNAMO sample (Green et al. 2014) and a sample of dwarf galaxies from Moiseev et al. (2015). In each panel, the different symbols of the top left corner refer to the data from different references.

Table 3. The results of the linear correlation analysis.

	$\sigma - \mathrm{SFR}$			$\sigma - \mathrm{M_*}$			$\sigma - \Sigma_{\mathrm{SFR}}$			$\sigma - \Sigma_*$		
	R_S	P	R_B	R_S	P	R_B	R_S	P	R_B	R_S	P	R_B
MaNGA+High z	0.70	<0.001	0.68	0.34	<0.001	0.33	0.67	<0.001	0.64	0.43	<0.001	0.41

Note: R_S: Spearman correlation coefficient.

P: Significance level of the Spearman correlation coefficient.

R_P: Pearson correlation coefficient.

and SFR, also a similarly weak correlation with Σ_{SFR}, but a moderate correlation is found between the dispersion and stellar mass. They argued that gaseous disks of high redshift star-forming galaxies are significantly different from those in local Universe, with the former showing much hotter dynamics. They suggested that feedback may not be a dominant contributor to their turbulence, but instead the discs may keep their turbulence through ongoing disc instabilities or continuous accretion of cold clumpy gas from the cosmic web (Kereš et al. 2005; Dekel, Sari & Ceverino 2009). The difference between the work of Stott et al. (2016) and the work of Johnson et al. (2018) is the way to measure the gas velocity dispersion and different theory to remove beam smearing.

Johnson et al. (2018) also used KROSS sample to study the relations of gas velocity dispersion versus stellar mass and SFR. They found that before removing the effect of the beam smearing, the average velocity dispersion increases significantly with the stellar mass. But the relation disappeared after removing the beam smearing, instead the dispersions increase with redshift at fixed stellar masses. There is a weak trend between the intrinsic velocity dispersion and SFR. Their results are consistent with an evolution of galaxy dynamics in which gas-rich disks are increasingly gravitationally unstable at higher redshift.

Green et al. (2010) and Johnson et al. (2018) combined with local galaxies and high-z galaxies, and found that the gas velocity dispersions are correlated with their SFRs, but not with their masses or gas fractions. They suggested that star formation is the energetic driver of galaxy disk turbulence at all cosmic epochs. Green et al. (2014) used DYNAMO sample, combined with high-redshift

galaxies, and revisited the relation between velocity dispersion and SFR, also found the similar relation.

In our study, the MaNGA survey makes available a much larger sample of nearby galaxies. Combined with high-z samples compiled from the literature, we have a larger sample than previous works. From the results of these wide redshift samples, we found that the relationships of the velocity dispersion with SFR as well as Σ_{SFR} may be more fundamental than with stellar mass and Σ_*. The latter may be caused by the former combined with the fact that the stellar masses could regulate SFRs to some extent (Shi et al. 2011, 2018).

4.2 Theoretical models to explain the relation between σ_{gas} and SFR

There are two dominant models for the origin of the turbulence: star formation feedback or gravitational instability of the gas (Krumholz & Burkhart 2016). Both models predict that the velocity dispersions will correlate with their SFRs. The work of Krumholz & Burkhart (2016) gives the details about these two models.

In Fig. 8, we overlaid the gravitational-instability model (left-hand panel) and star-formation-feedback model (right-hand panel). The gravitational-instability model gives SFR as following (Krumholz & Burkhart 2016):

$$\mathrm{SFR} = \int_{r_0}^{r_1} 2\pi r \epsilon_{\mathrm{ff}} \frac{\Sigma}{t_{\mathrm{ff}}} \, \mathrm{d}r = \frac{16}{\pi} \sqrt{\frac{\phi_P}{3}} \left(\frac{\epsilon_{\mathrm{ff}} v_c^2}{G} \ln \frac{r_1}{r_0} \right) f_g^2 \sigma. \tag{3}$$

where v_c is the rotational velocity, f_g is the gas fraction, $\epsilon_{\mathrm{ff}} = 0.01$ is the SFR per free-fall time, $\phi_P = 3$ is a factor that accounts for the presence of stars in the disc, and a Coulomb logarithm-
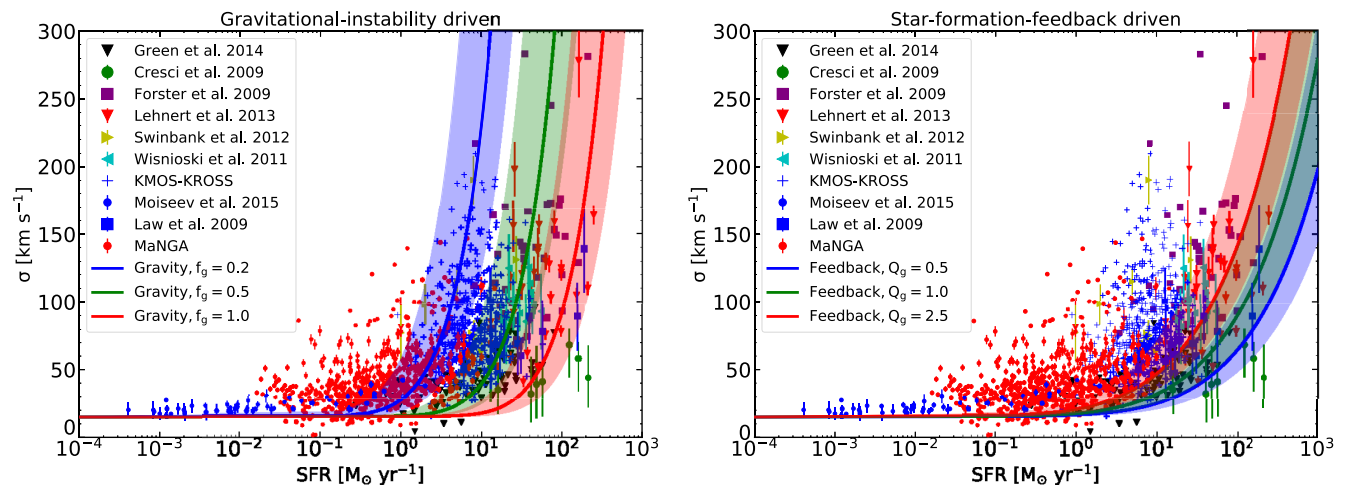

Figure 8. The relationship between SFR and gas velocity dispersion. In the left-hand panel, lines show the predictions of the gravitational-instability model (equation 6) for $f_g = 0.2$, 0.5, and 1.0, as indicated in the legend. Lines in the right panel show the prediction of the star formation feedback model (equation 8) for $Q_g = 0.5$, 1.0, and 2.5. The solid lines are for a circular velocity $v_c = 140 \, km\,s^{-1}$ (the median rotation velocity of local and high z galaxies), and the shaded range shows values from $v_c = 90–190 \, km\,s^{-1}$, which spans the plausible range for the local and high-redshift samples. Note that the theoretical model predictions for σ have been added in quadrature with the thermal broadening of HII region about $15 \, km\,s^{-1}$.

like term $\ln(r_1/r_0)$, which measures the radial extent of the star-forming disc ($r_1 = 10$, $r_0 = 0.1$). From equation (3) we find that a gravitational-instability model has a strong dependence on the gas fraction. The star formation feedback model gives the SFR as following (Krumholz & Burkhart 2016):

$$\text{SFR} = \int_{r_0}^{r_1} 2\pi r \dot{\Sigma}_* \, dr = \frac{8\sqrt{2}\phi v_c^2}{\pi G Q_g \mathcal{F}} \left(\ln \frac{r_1}{r_0} \right) \left(\frac{P_*}{m_*} \right)^{-1} \sigma^2. \qquad (4)$$

where Q_g is the Toomre parameters of the gas, $\phi \approx 1$ and $\mathcal{F} \approx 2$ are constants of order unity that parametrize various uncertainties, $P_*/m_* = 3000$ km s^{-1} is the momentum per unit mass (Faucher-Giguère, Quataert & Hopkins 2013). We found that the star formation feedback origin for the turbulence predicts that a velocity dispersion rises more steeply with the SFR, and it does not depend on the gas fraction. For the comparisons with our observations, we give the plausible range of f_g and Q_g following with the works of Krumholz & Burkhart (2016) or Johnson et al. (2018). We also used the rotation velocity $v_c = 90$–190 km s^{-1}, which spans the plausible range for local and high z galaxies. From Fig. 8 (right panel), we find that a star-formation-feedback model provides a rather poor match to the observation, while the gravitational-instability model shows better agreement with the observations. Johnson et al. (2018) also test two analytic models but found that both provide an adequate description of the data, and need further observations to rule out either model. In the work of Krumholz & Burkhart (2016), they also compared with observations and found that gravity is the ultimate source of ISM turbulence, at least in rapidly star-forming, high-velocity dispersion galaxies for which our test is most effective.

The recent work of Krumholz et al. (2018), provided a new model for the structure and evolution of gas in galactic discs. For the relation between σ and SFR, they found that the transport+feedback model is in generally good agreement with the observations at both low and high SFRs. We compare our MaNGA data with their data and transport+feedback model in Fig. 9. It is shown that our MaNGA galaxies locate within the range between local dwarf and local spiral galaxies of their models' predictions (solid lines). A key parameter in their model for dwarf galaxies is the rotation velocity which is adopted to be 100 km s^{-1}. Fig. 10 shows the distribution of the rotation velocity of our MaNGA galaxies, which is about 90 ± 50 km s^{-1}, consistent with their values for dwarf galaxies. This may explain our galaxies are better fitted by their dwarf-galaxy model. Overall, Fig. 9 suggests that the transport+feedback model does a good job in matching our data.

4.3 Theoretical models to explain the relation between σ_{gas} and Σ_{SFR}

Fig. 11 shows the relationship between σ_{gas} and Σ_{SFR}. We attempt to use theoretical models to explain this relation. If the Jeans instability drives the clumpiness of the discs, there is expected to be a good correlation between the mass of collapsing gas and the gas velocity dispersion (Elmegreen et al. 2007). Assuming the turbulence is powered by gravity, Lehnert et al. (2009) derived a simple Jeans relationship between gas velocity dispersion and mass:

$$\sigma_{gas} \sim M_J^{1/4} G^{1/2} \Sigma_{gas}^{1/4} = 54 M_{J,9}^{1/4} \Sigma_{\text{SFR}}^{0.18} \text{ km s}^{-1} \qquad (5)$$

where G is the gravitational constant, $M_{J,9}$ is Jeans mass in 10^9 M$_\odot$ and Σ_{SFR} is the surface density of SFR in unites M$_\odot$ kpc^2 yr^{-1}. In Fig. 11, the red solid line shows the relationship between σ_{gas} and Σ_{SFR} of a 10^8 M$_\odot$ giant molecular cloud. Because the masses of our local star-forming galaxies are similar to the Milky Way,
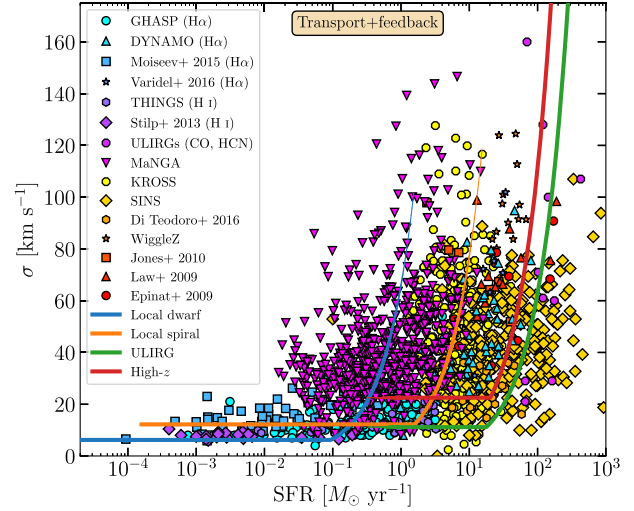

Figure 9. Comparison between the observed correlation between gas velocity dispersion and star formation rate and theoretical model. Solid lines represent the theoretical Transport+feedback model for Local dwarf, Local spiral, ULIRG and High-z galaxies. The coloured points represent observation datas. The local galaxies are from Epinat, Amram & Marcelin (2008) (GHASP), Green et al. (2010) (DYNAMO), Moiseev et al. (2015), Varidel et al. (2016); The HI observations of nearby galaxies from THINGS (Leroy et al. 2008; Walter et al. 2008; Ianjamasimanana et al. 2012) and Stilp et al. (2013). The nearby ULIRGs observations from Downes & Solomon (1998), Sanders et al. (2003), Veilleux et al. (2009) and Scoville et al. (2015, 2017). The high z galaxies are from Epinat et al. (2009), Law et al. (2009), Jones et al. (2010), Di Teodoro, Fraternali & Miller (2016); The WiggleZ sample is from Wisnioski et al. (2011); The SINS sample is from Wisnioski et al. (2015), Wuyts et al. (2016); The KMOS-KROSS sample is from Johnson et al. (2018). Full details about the data are given in Appendix B of Krumholz et al. (2018). The code of this plot is also from Krumholz et al. (2018).
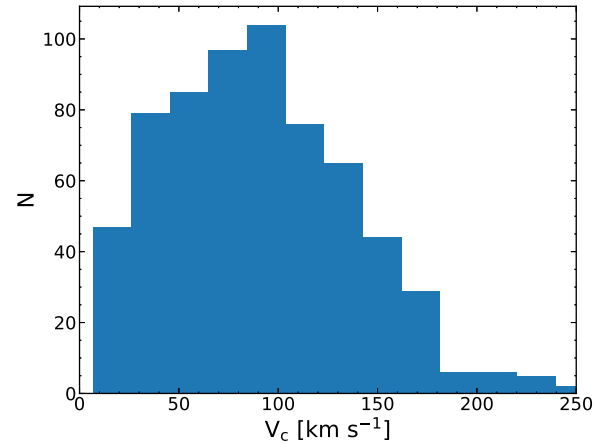

Figure 10. The distribution of galaxy rotation curve velocity v_c for MaNGA galaxies. The mean value is $v_c = 91.58$ km s^{-1}. The standard deviation of mean value is 50.83 km s^{-1}.

the masses of molecular cloud is impossible more than 10^8 M$_\odot$ (Roman-Duval et al. 2010). So we chose 10^8 M$_\odot$ as the upper limit on the possible contribution of the clumps to the observed velocity dispersion. Fig. 11 shows that the velocity dispersion predicted by equation (5) lies below the observed data. Lehnert et al. (2009) obtained the similar results for high-z galaxies. They selected 10^9 M$_\odot$ giant molecular cloud, which is the largest masses
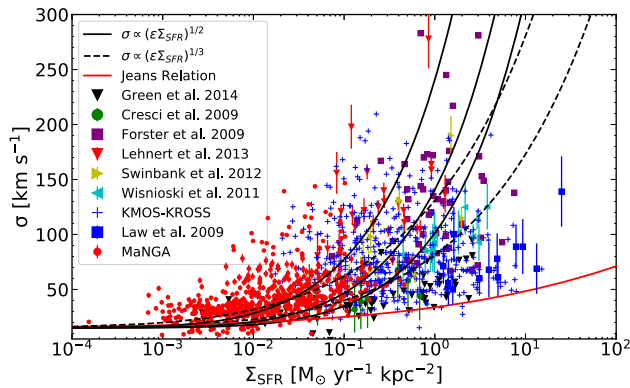
Figure 11. Plot of the $\sigma_{\rm gas}$ versus $\Sigma_{\rm SFR}$ in MaNGA sample and other local and high-z galaxies. The symbols for the different samples are shown in the legend to this figure. The solid black lines show that if star formation dominates the dissipated energy, we may expect the relationship of the form $\sigma \propto (\epsilon \dot{E})^{1/2}$, where ϵ is the coupling efficiency between the ISM and the energy injection, $\dot{E}$ is the energy injection due to the star formation. From bottom to top: $\sigma_{\rm gas} = 100\Sigma_{\rm SFR}^{1/2}$ km s^{-1}, $\sigma_{\rm gas} = 140\Sigma_{\rm SFR}^{1/2}$ km s^{-1} and $\sigma_{\rm gas} = 240\Sigma_{\rm SFR}^{1/2}$ km s^{-1}. The dashed lines show that if the dispersions correspond to energy dissipation due to turbulent motions, we have $\sigma \propto (\epsilon \dot{E})^{1/3}$. From bottom to top: $\sigma_{\rm gas} = 80\Sigma_{\rm SFR}^{1/3}$ km s^{-1} and $\sigma_{\rm gas} = 130\Sigma_{\rm SFR}^{1/3}$ km s^{-1}. The red solid line represents the velocity dispersion of a 10^8 M$_\odot$ clump using a simple Jeans relationship. Note that the theoretical model predictions for σ have been added in quadrature with the thermal broadening of HII region about 15 km s^{-1}.

estimated for clumps based on spectral energy distribution fitting for high-z galaxies. This comparison implies that the dispersions are not dominated by the self-gravity of the clumps.

Lehnert et al. (2009) pointed that, if star formation dominates the dissipated energy, we may expect a simple scaling law $\sigma \propto (\epsilon \dot{E})^{1/2}$, where ϵ is the coupling efficiency between the ISM and the energy injection, $\dot{E}$ is the energy injection due to star formation. Dib, Bell & Burkert (2006) noticed that if the coupling efficiency in the ISM modelling is 25 per cent, for galaxies at $\Sigma_{\rm SFR} = 10^{-2.5}$ to 10^{-2} M$_\odot$ yr^{-1} kpc^{-2} the disks change from quiescent to starburst ones. In Fig. 11, the bottom two solid black lines are derived from $\sigma_{\rm gas} = 100\Sigma_{\rm SFR}^{1/2}$ km s^{-1} and $\sigma_{\rm gas} = 140\Sigma_{\rm SFR}^{1/2}$ km s^{-1}, respectively, and the third black solid curve at the top shows $\sigma_{\rm gas} = 240\Sigma_{\rm SFR}^{1/2}$ km s^{-1} with coupling efficiencies of 100 per cent. If turbulent motions determines the observed velocity dispersions (Mac Low 1999), we may expect another scaling law $\sigma \propto (\epsilon \dot{E})^{1/3}$, where $\dot{E}$ is the energy dissipated due to turbulence. In Fig. 11, the two black dashed lines are derived from $\sigma_{\rm gas} = 80\Sigma_{\rm SFR}^{1/3}$ km s^{-1} and $\sigma_{\rm gas} = 130\Sigma_{\rm SFR}^{1/3}$ km s^{-1}, using two scalings for the coupling efficiency, 25 per cent and 100 per cent and a primary injection scale of 1 kpc. From Fig. 11 we found that both $\sigma \propto (\epsilon \dot{E})^{1/2}$ and $\sigma \propto (\epsilon \dot{E})^{1/3}$, provide an adequate description of the data. But the value of the coupling efficiencies of 100 per cent is an extreme and unrealistic value (the top solid line and the top dashed line in Fig. 11). The energy source of turbulence of galaxies with high velocity dispersions may have multiple origins and star formation alone is insufficient to explain it.

5 CONCLUSIONS

In this work, we have analysed the intrinsic velocity dispersion properties of 648 MaNGA star-forming galaxies, and combined them with high-z galaxies. Our main results are as follows:

(1) There is a good correlation between the velocity dispersion and SFR as well as $\Sigma_{\rm SFR}$. But there is just a moderate correlation between the velocity dispersion and stellar mass as well as Σ_*.

(2) Comparing theoretical models with observations, because of the different model assumptions, we found that star formation feedback alone and gravitational instability alone cannot reproduce the observed two relationships (velocity dispersions versus SFRs and velocity dispersions versus $\Sigma_{\rm SFR}$). These different models imply that gas fraction may be an important parameter in this topic.

REFERENCES

Baldwin J. A., Phillips M. M., Terlevich R., 1981, PASP, 93, 5
Blanton M. R. et al., 2017, AJ, 154, 28
Bournaud F. et al., 2014, ApJ, 780, 57
Bournaud F., Elmegreen B. G., Teyssier R., Block D. L., Puerari I., 2010, MNRAS, 409, 1088
Bryant J. J., Bland-Hawthorn J., Fogarty L. M. R., Lawrence J. S., Croom S. M., 2014, MNRAS, 438, 869
Bundy K. et al., 2015, ApJ, 798, 7
Burgarella D. et al., 2013, A&A, 554, A70
Calzetti D., 2001, PASP, 113, 1449
Cappellari M., 2017, MNRAS, 466, 798
Cappellari M., Emsellem E., 2004, PASP, 116, 138
Chabrier G., 2003, PASP, 115, 763

Chang Y.-Y., van der Wel A., da Cunha E., Rix H.-W., 2015, ApJS, 219, 8
Chen Y.-M. et al., 2016, NatCo, 7, 13269
Cresci G. et al., 2009, ApJ, 697, 115
Croom S. M. et al., 2012, MNRAS, 421, 872
Davies R. et al., 2011, ApJ, 741, 69
Dekel A., Sari R., Ceverino D., 2009, ApJ, 703, 785
Di Teodoro E. M., Fraternali F., Miller S. H., 2016, A&A, 594, A77
Dib S., Bell E., Burkert A., 2006, ApJ, 638, 797
Downes D., Solomon P. M., 1998, ApJ, 507, 615
Drory N. et al., 2015, AJ, 149, 77
Elmegreen B. G., Burkert A., 2010, ApJ, 712, 294
Elmegreen D. M., Elmegreen B. G., Ravindranath S., Coe D. A., 2007, ApJ, 658, 763
Epinat B. et al., 2009, A&A, 504, 789
Epinat B., Amram P., Marcelin M., 2008, MNRAS, 390, 466
Epinat B., Amram P., Balkowski C., Marcelin M., 2010, MNRAS, 401, 2113
Faucher-Giguère C.-A., Quataert E., Hopkins P. F., 2013, MNRAS, 433, 1970
Federrath C., Klessen R. S., 2012, ApJ, 761, 156
Förster Schreiber N. M. et al., 2009, ApJ, 706, 1364
Genzel R. et al., 2011, ApJ, 733, 101
Glazebrook K., 2013, PASA, 30, e056
Goldbaum N. J., Krumholz M. R., Forbes J. C., 2015, ApJ, 814, 131
Gonçalves T. S. et al., 2010, ApJ, 724, 1373
Green A. W. et al., 2010, Natur, 467, 684
Green A. W. et al., 2014, MNRAS, 437, 1070
Green A. W. et al., 2018, MNRAS, 475, 716
Gunn J. E. et al., 2006, AJ, 131, 2332
Harrison C. M. et al., 2016, MNRAS, 456, 1195
Hopkins A. M., Beacom J. F., 2006, ApJ, 651, 142
Ianjamasimanana R., de Blok W. J. G., Walter F., Heald G. H., 2012, AJ, 144, 96
Jin Y. et al., 2016, MNRAS, 463, 913
Johnson H. L. et al., 2018, MNRAS, 474, 5076
Jones T. A., Swinbank A. M., Ellis R. S., Richard J., Stark D. P., 2010, MNRAS, 404, 1247
Karim A. et al., 2011, ApJ, 730, 61
Kauffmann G. et al., 2003, MNRAS, 346, 1055
Kelly B. C., 2007, ApJ, 665, 1489
Kennicutt R. C., Jr, 1998, ARA&A, 36, 189
Kereš D., Katz N., Weinberg D. H., Davé R., 2005, MNRAS, 363, 2
Kewley L. J., Groves B., Kauffmann G., Heckman T., 2006, MNRAS, 372, 961
Kewley L. J., Dopita M. A., Leitherer C., Davé R., Yuan T., Allen M., Groves B., Sutherland R., 2013, ApJ, 774, 100
Krumholz M. R., Burkhart B., 2016, MNRAS, 458, 1671
Krumholz M. R., Burkhart B., Forbes J. C., Crocker R. M., 2018, MNRAS, 477, 2716
Law D. R. et al., 2015, AJ, 150, 19
Law D. R. et al., 2016, AJ, 152, 83
Law D. R., Steidel C. C., Erb D. K., Larkin J. E., Pettini M., Shapley A. E., Wright S. A., 2007, ApJ, 669, 929
Law D. R., Steidel C. C., Erb D. K., Larkin J. E., Pettini M., Shapley A. E., Wright S. A., 2009, ApJ, 697, 2057
Le Tiran L., Lehnert M. D., van Driel W., Nesvadba N. P. H., Di Matteo P., 2011, A&A, 534, L4
Lehnert M. D., Nesvadba N. P. H., Le Tiran L., Di Matteo P., van Driel W., Douglas L. S., Chemin L., Bournaud F., 2009, ApJ, 699, 1660

Lehnert M. D., Le Tiran L., Nesvadba N. P. H., van Driel W., Boulanger F., Di Matteo P., 2013, A&A, 555, A72
Leroy A. K., Walter F., Brinks E., Bigiel F., de Blok W. J. G., Madore B., Thornley M. D., 2008, AJ, 136, 2782
Lilly S. J., Le Fevre O., Hammer F., Crampton D., 1996, ApJ, 460, L1
Mac Low M.-M., 1999, ApJ, 524, 169
Mac Low M.-M., Klessen R. S., Burkert A., Smith M. D., 1998, PhRvL, 80, 2754
Madau P., Dickinson M., 2014, ARA&A, 52, 415
Madau P., Ferguson H. C., Dickinson M. E., Giavalisco M., Steidel C. C., Fruchter A., 1996, MNRAS, 283, 1388
Moiseev A. V., Tikhonov A. V., Klypin A., 2015, MNRAS, 449, 3568
Nesvadba N. P. H., Lehnert M. D., Eisenhauer F., Gilbert A., Tecza M., Abuter R., 2006, ApJ, 650, 693
Roman-Duval J., Jackson J. M., Heyer M., Rathborne J., Simon R., 2010, ApJ, 723, 492
Salim S. et al., 2016, ApJS, 227, 2
Sánchez S. F. et al., 2012, A&A, 538, A8
Sánchez S. F. et al., 2016, RMxAA, 52, 171
Sánchez S. F. et al., 2016, RMxAA, 52, 21a
Sanders D. B., Mazzarella J. M., Kim D.-C., Surace J. A., Soifer B. T., 2003, AJ, 126, 1607
Scoville N. et al., 2015, ApJ, 800, 70
Scoville N. et al., 2017, ApJ, 836, 66
Sharp R. et al., 2015, MNRAS, 446, 1551
Shi Y. et al., 2018, ApJ, 853, 149
Shi Y., Helou G., Yan L., Armus L., Wu Y., Papovich C., Stierwalt S., 2011, ApJ, 733, 87
Simons R. C. et al., 2017, ApJ, 843, 46
Smee S. A. et al., 2013, AJ, 146, 32
Sobral D., Smail I., Best P. N., Geach J. E., Matsuda Y., Stott J. P., Cirasuolo M., Kurk J., 2013, MNRAS, 428, 1128
Stilp A. M., Dalcanton J. J., Skillman E., Warren S. R., Ott J., Koribalski B., 2013, ApJ, 773, 88
Stone J. M., Ostriker E. C., Gammie C. F., 1998, ApJ, 508, L99
Stott J. P. et al., 2016, MNRAS, 457, 1888
Swinbank A. M., Smail I., Sobral D., Theuns T., Best P. N., Geach J. E., 2012, ApJ, 760, 130
Tasker E. J., Tan J. C., 2009, ApJ, 700, 358
Varidel M., Pracy M., Croom S., Owers M. S., Sadler E., 2016, PASA, 33, e006
Veilleux S. et al., 2009, ApJS, 182, 628
Wake D. A. et al., 2017, AJ, 154, 86
Walter F., Brinks E., de Blok W. J. G., Bigiel F., Kennicutt R. C., Jr., Thornley M. D., Leroy A., 2008, AJ, 136, 2563
Westfall K. B. et al., 2019, preprint (arXiv:1901.00856)
Wisnioski E. et al., 2011, MNRAS, 417, 2601
Wisnioski E. et al., 2015, ApJ, 799, 209
Wuyts S. et al., 2016, ApJ, 831, 149
Yan R. et al., 2016, AJ, 151, 8
Yan R. et al., 2016, AJ, 152, 197
Zhou L. et al., 2017, MNRAS, 470, 4573

This paper has been typeset from a TEX/LATEX file prepared by the author.